Check for updates

Experimental investigation in nodal aberration theory (NAT) with a customized Ritchey-Chrétien system: third-order coma

NAN ZHAO,[1,2,3,*] **JONATHAN C. PAPA,**[3] **KYLE FUERSCHBACH,**[3] **YANFENG QIAO,**[1] **KEVIN P. THOMPSON,**[3,4,5] **AND JANNICK P. ROLLAND**[3]

[1]*Changchun Institute of Optics, Fine Mechanics and Physics, Chinese Academy of Sciences, Changchun, Jilin, 130033, China*
[2]*University of Chinese Academy of Sciences, Beijing, 100049, China*
[3]*The Institute of Optics, University of Rochester, Rochester, NY 14620, USA*
[4]*Synopsys, Inc., 3 Graywood Lane, Pittsford, NY 13145, USA*
[5]*Deceased*
[*]*zhaonan@ciomp.ac.cn*

Abstract: Nodal aberration theory (NAT) describes the aberration properties of optical systems without symmetry. NAT was fully described mathematically and investigated through real-ray tracing software, but an experimental investigation is yet to be realized. In this study, a two-mirror Ritchey-Chrétien telescope was designed and built, including testing of the mirrors in null configurations, for experimental investigation of NAT. A feature of this custom telescope is a high-precision hexapod that controls the secondary mirror of the telescope to purposely introduce system misalignments and quantify the introduced aberrations interferometrically. A method was developed to capture interferograms for multiple points across the field of view without moving the interferometer. A simulation result of Fringe Zernike coma was generated and analyzed to provide a direct comparison with the experimental results. A statistical analysis of the measurements was conducted to assess residual differences between simulations and experimental results. The interferograms were consistent with the simulations, thus experimentally validating NAT for third-order coma.

References and links

1. H. H. Hopkins, *The Wave Theory of Aberrations* (Oxford on Clarendon, 1950).
2. R. V. Shack and K. P. Thompson, "Influence of alignment errors of a telescope system on its aberration field," Proc. SPIE **251**, 146–153 (1980).
3. K. Thompson, "Description of the third-order optical aberrations of near-circular pupil optical systems without symmetry," J. Opt. Soc. Am. A **22**(7), 1389–1401 (2005).
4. K. P. Thompson, "Multinodal fifth-order optical aberrations of optical systems without rotational symmetry: spherical aberration," J. Opt. Soc. Am. A **26**(5), 1090–1100 (2009).
5. K. P. Thompson, "Multinodal fifth-order optical aberrations of optical systems without rotational symmetry: the comatic aberrations," J. Opt. Soc. Am. A **27**(6), 1490–1504 (2010).
6. K. P. Thompson, "Multinodal fifth-order optical aberrations of optical systems without rotational symmetry: the astigmatic aberrations," J. Opt. Soc. Am. A **28**(5), 821–836 (2011).
7. K. Fuerschbach, J. P. Rolland, and K. P. Thompson, "Theory of aberration fields for general optical systems with freeform surfaces," Opt. Express **22**(22), 26585–26606 (2014).
8. J. R. Rogers, "Origins and fundamentals of nodal aberration theory," in *Optical Design and Fabrication 2017 (IODC, Freeform, OFT)*, OSA Technical Digest (online) (Optical Society of America, 2017), paper JTu1C.1.
9. J. W. Figoski, T. E. Shrode, and G. F. Moore, "Computer-aided alignment of a wide-filed, three-mirror, unobscured, high-resolution sensor," Proc. SPIE **1049**, 166–177 (1989).
10. R. A. Buchroeder, "Tilted component optical systems," Ph.D. dissertation (University of Arizona, 1976).
11. K. P. Thompson, T. Schmid, O. Cakmakci, and J. P. Rolland, "Real-ray-based method for locating individual surface aberration field centers in imaging optical systems without rotational symmetry," J. Opt. Soc. Am. A **26**(6), 1503–1517 (2009).

12. D. Malacara, *Optical Shop Testing*, 3rd ed. (John Wiley & Sons, Inc., 2007), Chap. 12.
13. T. Yang, J. Zhu, and G. Jin, "Nodal aberration properties of coaxial imaging systems using Zernike polynomial surfaces," J. Opt. Soc. Am. A **32**(5), 822–836 (2015).
14. J. C. Wyant and K. Creath, "Basic wavefront aberration theory for optical metrology," in *Applied Optics and Optical Engineering*, R. R. Shannon and J. C. Wyant, eds. (Academic, 1992).
15. J. C. DeBruin and D. B. Johnson, "Image rotation in plane-mirror optical systems," Proc. SPIE **1696**, 41–59 (1992).
16. CODE V reference manual, Version 11.0, 2017, Synopsys, Inc.
17. MetroPro manual, Version 9.0, 2011, Zygo Corporation, http://www.zygo.com.
18. X. Hou, F. Wu, L. Yang, and Q. Chen, "Comparison of annular wavefront interpretation with Zernike circle polynomials and annular polynomials," Appl. Opt. **45**(35), 8893–8901 (2006).
19. T. Schmid, K. P. Thompson, and J. P. Rolland, "A unique astigmatic nodal property in misaligned Ritchey-Chrétien telescopes with misalignment coma removed," Opt. Express **18**(5), 5282–5288 (2010).
20. T. Schmid, J. P. Rolland, A. Rakich, and K. P. Thompson, "Separation of the effects of astigmatic figure error from misalignments using nodal aberration theory (NAT)," Opt. Express **18**(16), 17433–17447 (2010).
21. T. Schmid, "Misalignment induced nodal aberration fields and their use in the alignment of astronomical telescopes," Ph.D. dissertation (University of Central Florida, Orlando, Florida, 2010).

1. Introduction

Nodal aberration theory (NAT), discovered by R.V. Shack in 1977, is based on the wave aberration theory of Hopkins [1, 2] and was developed to fifth-order by K. P. Thompson [3–6]. The theory provides a complete mathematical description of the aberration properties in misaligned or arbitrarily decentered and tilted optical systems under the assumption that the system components are inherently rotationally symmetric. Recently, of significance to the importance of NAT, was showing that an expansion of NAT led to the aberrations induced by freeform surfaces [7]. A key discovery of NAT is that aberrations display nodal behaviors related to their field dependence when the symmetry of the system is broken, as reviewed and highlighted by John Rogers in a memorial address to Kevin Thompson [8].

Experimental investigation of this insightful theory has not yet been developed. In this paper, we report on the design and assembly of a customized Ritchey–Chrétien telescope specifically built to experimentally investigate NAT whose secondary mirror is controlled by a hexapod to create an arbitrarily misaligned system. The telescope development from design to full assembly was launched in 2010 in Memoriam of Robert S. Hilbert, thus the so-called 'Hilbert telescope'. To interferometrically capture the wavefront aberrations at different field points without moving the interferometer is an interesting practical problem which was solved by Figoski et. al. by a double-pass optical layout and a phase modulator controlled remotely [9].

In this paper, a double-pass layout and field generator were conceived and described to also capture interferograms at multiple points in the field without moving any interferometer or system under test, which can be applied to other systems facing this challenge. In Section 2, we will first briefly review the nodal properties of third-order coma in optical systems without symmetry. In Section 3, we will elaborate on the optical and optomechanical design and assembly for the Hilbert telescope. In Section 4, the experimental methods will be laid out together with simulations. In Section 5, experimental results pertaining to the coma aberration will be presented and compared to the simulations. In section 6, a data analysis quantifies the accuracy of the simulations accounting for the obscuration and a statistical analysis quantifies the expected uncertainty in the measurements. Finally, future plans are given in section 7 before we conclude in Section 8.

2. Nodal property of third-order coma in optical systems without symmetry

For third-order aberrations in an optical system without symmetry, the vector form of the wave aberration expansion can be written as

$$W = \sum_j W_{040j} (\boldsymbol{\rho} \cdot \boldsymbol{\rho})^2 + \sum_j W_{131j} \left[(\boldsymbol{H} - \boldsymbol{\sigma}_j) \cdot \boldsymbol{\rho} \right] (\boldsymbol{\rho} \cdot \boldsymbol{\rho}) + \sum_j W_{222j} \left[(\boldsymbol{H} - \boldsymbol{\sigma}_j) \cdot \boldsymbol{\rho} \right]^2$$
$$+ \sum_j W_{220j} \left[(\boldsymbol{H} - \boldsymbol{\sigma}_j) \cdot (\boldsymbol{H} - \boldsymbol{\sigma}_j) \right] (\boldsymbol{\rho} \cdot \boldsymbol{\rho}) + \sum_j W_{311j} \left[(\boldsymbol{H} - \boldsymbol{\sigma}_j) \cdot (\boldsymbol{H} - \boldsymbol{\sigma}_j) \right] \left[(\boldsymbol{H} - \boldsymbol{\sigma}_j) \cdot \boldsymbol{\rho} \right], \tag{1}$$

where $\boldsymbol{H}$ denotes the normalized vector of the field coordinate on the image plane and $\boldsymbol{\rho}$ denotes the normalized vector of the pupil coordinate on the exit pupil plane, $\boldsymbol{\sigma}_j$ denotes the deviation in the center of the aberration field associated with surface j with respect to the unperturbed field center (center of the Gaussian image plane) [10,11]. The second summation in Eq. (1) is third-order coma, in which W_{131j} designates the wave aberration term contribution for third-order coma of surface j. It can be written as

$$W = \sum_j W_{131j} \left[(\boldsymbol{H} - \boldsymbol{\sigma}_j) \cdot \boldsymbol{\rho} \right] (\boldsymbol{\rho} \cdot \boldsymbol{\rho}) = \left\{ \left[\left(\sum_j W_{131j} \boldsymbol{H} \right) - \left(\sum_j W_{131j} \boldsymbol{\sigma}_j \right) \right] \cdot \boldsymbol{\rho} \right\} (\boldsymbol{\rho} \cdot \boldsymbol{\rho}). \tag{2}$$

The first summation in Eq. (2) is the contribution of the rotationally symmetric system, which can be written as

$$\sum_j W_{131j} \boldsymbol{H} = W_{131} \boldsymbol{H}. \tag{3}$$

The second summation in Eq. (2) can be considered as the sum of the contributions of the decentration vectors in the image plane associated with each surface and weighted by the corresponding third-order coma terms. Let's denote $\boldsymbol{A}_{131}$, the net, unnormalized vector in the image plane as

$$\boldsymbol{A}_{131} \equiv \sum_j W_{131j} \boldsymbol{\sigma}_j, \tag{4}$$

and the normalized vector, $\boldsymbol{a}_{131}$, as

$$\boldsymbol{a}_{131} \equiv \frac{\boldsymbol{A}_{131}}{W_{131}}, \tag{5}$$

where W_{131} is the system nominal wave aberration for third-order coma before misalignment. Equation (6) describes third-order coma in the field dependence of a misaligned system as

$$W = W_{131} \left[(\boldsymbol{H} - \boldsymbol{a}_{131}) \cdot \boldsymbol{\rho} \right] (\boldsymbol{\rho} \cdot \boldsymbol{\rho}). \tag{6}$$

Third-order coma maintains a linear dependence with the field $\boldsymbol{H}$ when the symmetry of the optical system is broken but the aberration center in the image plane is determined by the vector $\boldsymbol{a}_{131}$, generally no longer in the field center as illustrated in Fig. 1.
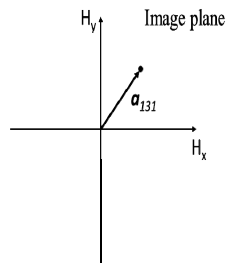

Fig. 1. The aberration field center of third-order coma in a misaligned system is denoted by $\boldsymbol{a}_{131}$.

A special case is when third-order coma is corrected in the nominal design, such as in a Ritchey-Chrétien system, where W_{131} is zero. In this case, the induced misalignment will result in the well-known constant coma across the field of view expressed as

$$W = -\left(A_{131} \cdot \rho\right)\left(\rho \cdot \rho\right),\tag{7}$$

where the vector A_{131} relates to the decentration vector σ_j in both magnitude and orientation, without dependence on field H, and indicates field constant coma across the field. A Cassegrain (Figs. 2(a) and 2(b)) and a Ritchey-Chrétien (Figs. 2(c) and 2(d)) telescopes were chosen to illustrate the nodal properties elaborated above, in the form of full field displays (FFDs) of Fringe Zernike coma ($Z_{7/8}$), which is significant in the layout pattern rather than the absolute value of aberrations as represented by the magnitude of the cones. We illustrate here in Figs. 2(a) and 2(c) the aligned states, with third-order coma initially either uncorrected or corrected as in a Cassegrain and Ritchey-Chrétien telescopes, respectively. Figures 2(b) and 2(d) demonstrate the field dependent coma with a 0.5 mm decenter of the secondary mirror with respect to the primary. In this case, the node of third-order coma is off-centered in the Cassegrain telescope as shown in Fig. 2(b), while the Ritchey-Chrétien telescope displays field constant coma shown in Fig. 2(d).
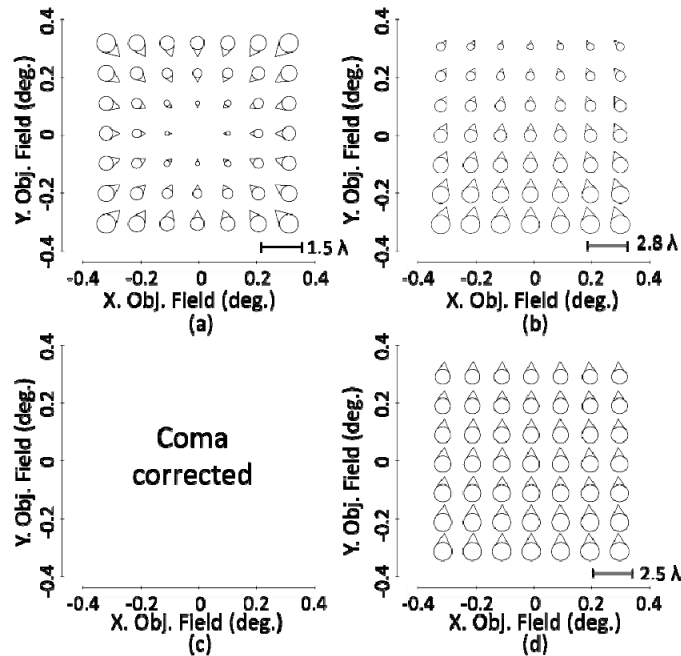

Fig. 2. Full Field Displays (FFDs) of Fringe Zernike coma $Z_{7/8}$ in a Cassegrain system (a-b) and a Ritchey-Chrétien system (c-d). (a) and (c) are the systems in aligned states. (b) and (d) are the corresponding systems with a 0.5 mm decenter in their secondary mirrors, respectively.

3. Hilbert telescope

3.1 Optical design and testing

To demonstrate these nodal properties, the Hilbert telescope was developed whose primary and secondary mirrors are −1291.2 mm and −425 mm in radii, respectively. Both primary and secondary mirrors are conic surfaces whose conic constants are −1.06 and −3.3095, respectively. The system specifications are listed in Table 1, and the schematic optical layout is shown in Fig. 3.

The primary and secondary mirrors were both tested in the lab with a phase-shifting Fizeau interferometer (DynaFiz from Zygo) using custom null optics [12]. Specifically, an Offner null lens (enlarged view in Fig. 4(a)) was designed to test the primary mirror. The Offner is composed of a corrector lens and a field lens, both of which are spherical optics. The corrector lens provides the correct amount of third-order spherical aberration to null that of the primary mirror, and the field lens images the corrector on to the primary mirror to suppress any induced higher order aberrations. A Hindle sphere was designed as an auxiliary test for the secondary mirror. The center of curvature of the Hindle sphere was made coincident with one of the foci of the hyperbolic secondary mirror. As the figure error of the Hindle sphere was included in the test, the result of secondary mirror shown here was the subtraction of the interferometer result and the figure error of the Hindle sphere, which was tested under the same mounting configuration. The null test setups and the results are shown in Figs. 4(a) and 4(b) for the primary and secondary mirror, respectively, where the color bar in the surface maps shows the peak-to-valley value of the interferogram. Results show an RMS surface figure error of 0.055 λ and 0.033 λ for the primary and secondary mirror, respectively, both at the testing wavelength of 632.8 nm. Results from experimental optical testing show that the figure errors on each mirror were limited to astigmatism and could be accounted for in the simulation model with Fringe Zernike coefficients ($Z_{5/6}$). Notably, however the study was focused on third-order coma, therefore the figure errors in the form of astigmatism had no impact on the interpreted results.

Table 1. Specifications of the Hilbert telescope

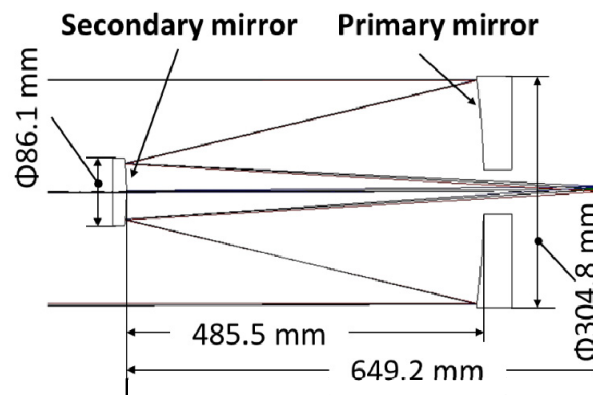| Parameter	Magnitude
Aperture (mm)	304.8
Wavelength (nm)	632.8
Full field of view (deg.)	± 0.15
Secondary obscuration (linear diameter)	28%
Focal length (mm)	2618.13
Overall length (mm)	561.7

Fig. 3. Schematic layout of the Hilbert telescope, a Ritchey-Chretien telescope by design.
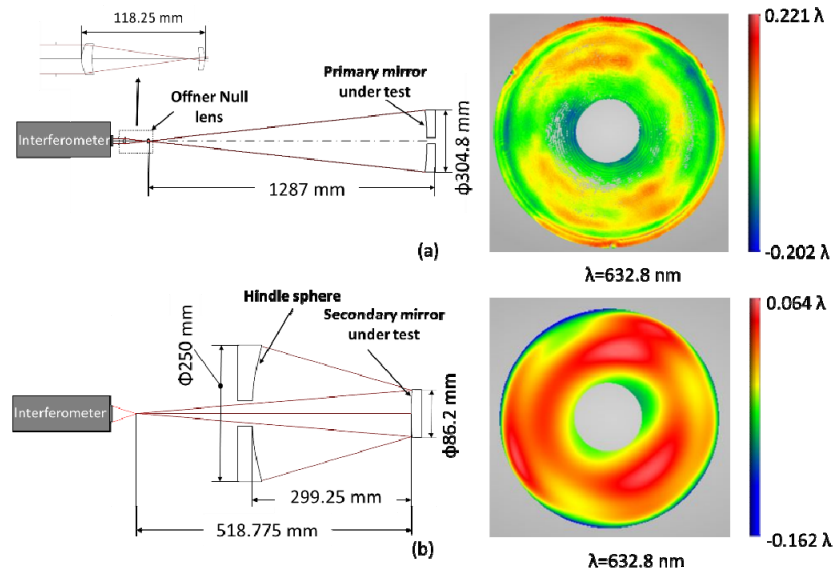
Fig. 4. Optical testing of the primary and secondary mirrors: (a) Primary mirror testing scheme (left) and surface figure error (right). (b) Secondary mirror testing scheme (left) and surface figure error (right).

3.2 Mechanical design

The Hilbert telescope was designed, built, and assembled to experimentally validate NAT, and we purposely decentered the secondary mirror to induce misalignment abberations. Thus, one of the key features of the mechanical design was the precise motion control of the secondary mirror. The primary mirror was held on an off-the-shelf mount (product from Edmund optics, part no. 36480). This mount had three actuators on the back to adjust the tip/tilt of the primary mirror that served as the reference for the assembly, which was noted as the primary bench.

To finely control the misalignment of the secondary mirror, it was mounted on a hexapod (PI instrumental, Model H-810). The hexapod has six degrees of freedom. Its specifications are listed in Table 2. A mirror mount and an adaptor were utilized to connect the secondary mirror to the hexapod. The secondary mirror assembly (SMA) is shown in Fig. 5(a). The total mass of the SMA was 2.2 kg. The structure to connect the SMA to the primary bench was another key design feature. Different supporting structures were compared in the difficulty of assembly and alignment, diffraction effects, and light obscuration, as well as the cost of implementation. A metering structure was conceived that consisted of eight truss tubes, an intermediate cylindrical baffle and a four-vane spider that provided enough stiffness to sustain the SMA and efficiently reduced the light obscuration. The outer diameter of the truss tubes was 1 in., with a wall thickness of 0.05 in., in the material of aluminum. While stiffer truss tubes were considered, the truss tubes chosen (i.e. off-the-shelf components) were sufficiently stiff that they resulted in a residual displacement for the secondary mirror that was small enough to be compensated with the hexapod as a calibration step. The spider was the bridge to connect the SMA to the baffle. The baffle was then supported by the primary bench through the truss tubes. The end of each truss tube was fixed with a ball that sat in a socket, which eased the assembly and alignment. The sockets were screwed separately to the primary bench and the baffle. Considering the diffraction effects, the four-vane spider was preferred as it rendered a cross-spike pattern, while a three-vane spider would render a six-spike diffraction pattern. To minimize the obscuration, the cylindrical baffle and truss tubes laid outside the clear aperture of the primary mirror, so the vanes and the SMA were the only

structures to obscure the light. Each vane was 1.4 mm in thickness, less than 0.5% in linear relative to the diameter of the primary mirror, which was almost negligible in the overall count for obscuration. The outer diameter of the SMA was 100 mm, which resulted in a 33% obscuration in linear diameter. The truss tubes, sockets with ball connection, and spider vanes were chosen as off-the-shelf components to lower the cost and accelerate the time to assembly. All parts mentioned above were labeled in Fig. 5(a). The assembled truss structure bears the load through tension and compression without relying on its bending stiffness.

Table 2. Main specifications of the hexapod

Travel range in X, Y (mm)	± 20
Travel range in Z (mm)	± 6.5
Travel range in θ_x, θ_Y (deg.)	± 10
Travel range in θ_z (deg.)	± 30
Single actuator design resolution (nm)	40
Minimum incremental motion in X and Y (μm)	1
Minimum incremental motion in Z (μm)	0.5
Minimum incremental motion in θ_x, θ_Y, θ_z (μrad)	10
Mass (kg)	1.7
Load capacity (kg)	5

A simplified model of the supporting structure was evaluated in Finite Element Analysis (FEA) and the result is shown in Fig. 5(b). Main concerns about the structure were the displacement of the SMA and the natural frequency of the entire telescope. In FEA, the primary bench was omitted, as it worked as the base and the reference of the displacement. The hexapod, the secondary mirror, and its mount were considered as a rigid body, which was simplified as a concentrated mass in the location of its mass center. The concentrated mass was set to be 2.5 kg with a redundancy consideration of 13.6%. The yellow-orange cone shape is the Rigid Body Element (RBE) 'RBE3′ connection between the concentrated mass and the adaptor. The RBE3 consisted of line masses that are dense and resemble a solid cone. The truss tubes were modeled as "Crod" which loaded through tension/compression. Other connections were also "RBE3". All materials were set to be Aluminum 6061. The analysis revealed that the secondary mirror had a maximum displacement of roughly 0.1 mm that was compensated by the hexapod during assembly rather than working to stiffen the structure to reduce the displacement at the expense of larger obscuration and costs. The fundamental frequency of the Hilbert telescope was around 50 Hz that was higher than the natural frequency of the working environment. The model and FEA were performed in Siemens NX UG (10.0 version). The assembled Hilbert telescope is shown in Fig. 6.
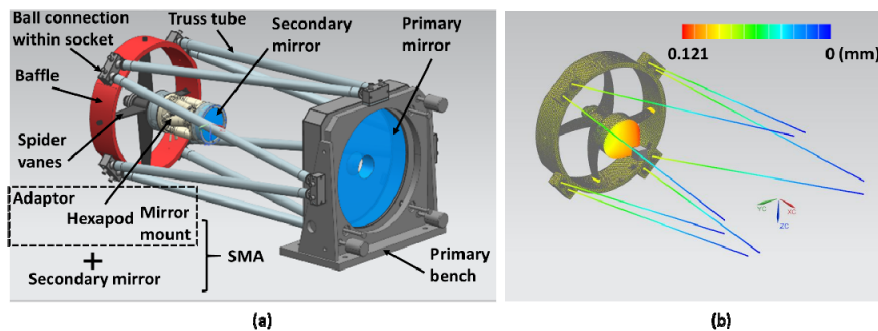

Fig. 5. Mechanical design model of the SMA assembly and attachment to the primary mirror: (a) Mechanical model of Hilbert telescope; (b) FE analysis result of displacement.
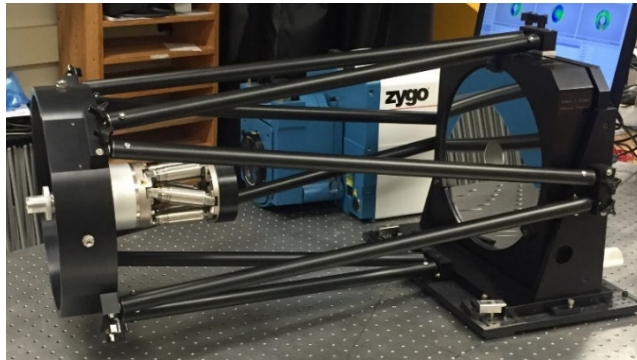
Fig. 6. The assembled Hilbert telescope.

4. Experiment setup and simulation results

To experimentally validate the nodal properties in the field dependence, it is necessary to measure the aberration content of the telescope at multiple points across the field. Furthermore, a wavefront measurement can illustrate aberrations in the form of Fringe Zernike coefficients that are well suited to compare against the simulation results. The experimental data will be measured interferometrically, as the interferometer is quantitative and sensitive to small variations.

4.1 Experiment setup and alignment

An experimental setup was conceived to involve a "field generator" and a "retro-reflector" in a double pass arrangement. The optical layout is shown in Fig. 7. The interferometer with a transmission sphere was collimated by a parabolic mirror that also served as the field generator of the Hilbert telescope as shown within the dash box on the right of Fig. 7. A high-quality fold mirror was required to reduce the optical path length for a more compact layout. Within the field generator was a tip/tilt mirror of 4 in. that generated the different fields and the parabolic mirror acted as the collimator. The tip/tilt mirror was placed at an angle of 45° relative to the optical axis whose mount was 120 mm in outer diameter, thus causing an obscuration of 85 mm. It is to be noted when the parabola is used off its optical axis, it creates field aberrations that will be quantified and subtracted. The interferometer was confocal with the parabolic mirror. The output beam from the interferometer was collimated after the field generator to the Hilbert telescope, with the outgoing angle to the collimated beam controlled by the tip/tilt mirror. The collimated beam then entered the Hilbert telescope. By varying the angle of the incoming beam, multiple field points of the Hilbert telescope were generated. A retro-reflector was placed in the image plane of the Hilbert telescope, which consisted of a convex-plano lens and a spherical mirror. The focus was adjusted with translation stages in three orthogonal directions X, Y, and Z to remain in focus for all points in the field. The adjustments of the tip/tilt mirror and retro-reflector were guided by real-ray tracing results in optical design software (i.e. CODE V). The travel range of the retro-reflector was 12 mm in each direction, which was controlled by three motorized actuators separately (product of Newport, model: TRA12CC). The actuator had an accuracy of ± 2.2 µm and a minimum incremental motion of 0.2 µm. The angle adjustment of the tip/tilt mirror was around one degree, executed manually by adjusting the tip/tilt mirror mount (product of Newport, model: U400-AC2K). The sensitivity of the tip/tilt mount was 1.3 arc sec. An example of nine points sampled across the field of view is listed in Table 3. The field points measured were constrained by the field of view of the Hilbert telescope and the translation range of the retro-reflector. The decentration amount was chosen to acquire stable interferograms against environmental turbulence.
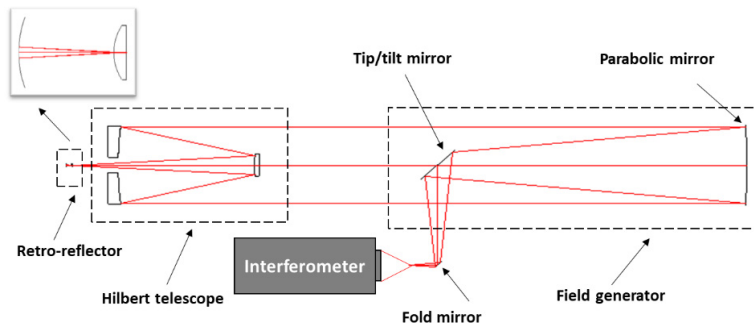
Fig. 7. Layout of the experimental setup for field measurements with the Hilbert telescope. The telescope was interfaced with a collimator that generates various points in the field of view of the telescope via a tip/tilt mirror and a retro-reflector that follows where the telescope is focusing.

Table 3. 3x3 grid of field points measured

(−0.1°, 0.1°)	(0°, 0.1°)	(0.1°, 0.1°)
(−0.1°, 0°)	(0°, 0°)	(0.1°, 0°)
(−0.1°, −0.1°)	(0°, −0.1°)	(0.1°, −0.1°)
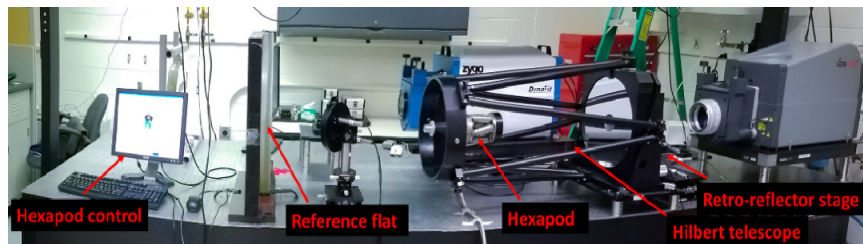
Fig. 8. The experiment setup captured during the alignment phase.

The entire system was on a vibration-isolation table, occupying a volume of approximately 3.6 m in length, 1.2 m in width, and 0.55 m in height as shown in Figs. 7 and 8. Two Fizeau interferometers with 4 in. apertures (DynaFiz and Verifire, Zygo) were used to aid in alignment and acquire interferograms of the wavefront. The interferometers were first made parallel by auto-collimating them to a 21 in. optical flat with the telescope structure in place including the primary mirror, but without the secondary in place as illustrated in Fig. 9.

Next, an optical axis was established, defined as the line that passes through the focus of the F/3.3 transmission sphere on the Verifire interferometer, which was also normal to the 21 in. optical flat. To ensure that the focus of the Verifire interferometer was placed at the correct location behind the primary mirror, the distance from the focus to the back of the primary, and the distance from the focus to the flat were measured. To align the primary mirror, a three-reflection configuration was used (see Fig. 10(a)), where the light from the Verifire interferometer reflected off the flat before being collimated by the primary, then auto-reflected off the flat before being focused by the primary. Small adjustments to the primary's position and orientation were made to remove tip, tilt, defocus, and coma in the measured interferogram.

After the primary mirror was aligned, the 21 in. flat was moved further from the primary, while maintaining its orientation using feedback from the Verifire interferometer with a transmission flat, through the hole in the primary. Then the secondary mirror was placed in the system (see Fig. 10(b)), and aligned by adjusting the hexapod to remove tip, tilt, defocus,

and coma in the interferogram. Then the parabola and fold mirrors were placed into the system and aligned to the telescope using feedback from the Dynafiz interferometer (see Fig. 11). A picture of the experiment is shown in Fig. 12.
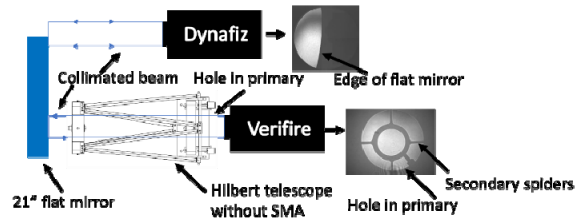

Fig. 9. Alignment of the two interferometers via auto-collimation on a 21 in. optical flat. The Dynafiz had a partially filled aperture. The Verifire was obscured by the hole in the primary and the secondary spiders. In this step of the alignment procedure, the Secondary Mirror Assembly (SMA) was removed.
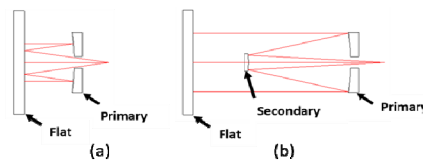
Fig. 10. (a) Alignment of the primary mirror of the Hilbert telescope to the reference 21 in. optical flat. (b) Alignment of the secondary mirror to the primary/flat combination.
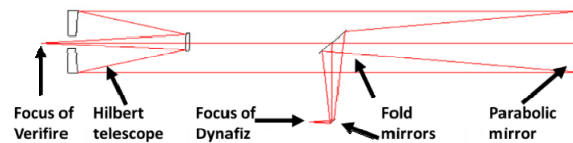
Fig. 11. Parabola aligned using the Dynafiz interferometer with a transmission sphere focus from which the beam was then collimated by the parabola, then focused at the focus of the Verifire (set by the transmission sphere of the Verifire) by the telescope, with the Verifire off, and returned. The fold mirrors and parabola were adjusted to remove tip, tilt, defocus, and coma in the Dynafiz interferogram.
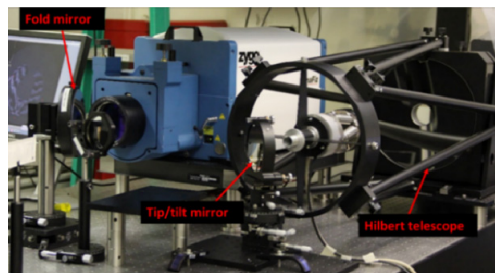
Fig. 12. The experimental setup with a zoom in view on the Hilbert telescope and tip-tilt mirror.

4.2 Simulation methods and results

A real ray trace model of the system and the pupil map analysis (PMA) feature in CODE V were used to obtain the optical path difference (OPD) data in the pupil for a 3 by 3 grid of field points (as specified in Table 3). Using MATLAB, the first 16 Fringe Zernike terms were fit to the OPD data with a normalization radius of 543.85 mm. The 7th and 8th Fringe Zernike terms were used to quantify the magnitude of coma using Eq. (8). Interferograms representing the magnitude and orientation of the coma for the 3 by 3 grid of field points in the aligned state can be seen in Fig. 13(a), Fig. 13(b) shows the interferograms for the misaligned state,

and Fig. 13(c) shows the subtraction of the aligned and misaligned OPD data to reveal field constant coma. Above each interferogram, the magnitude of the coma in waves is reported, where the wavelength is 632.8 nm [13,14].

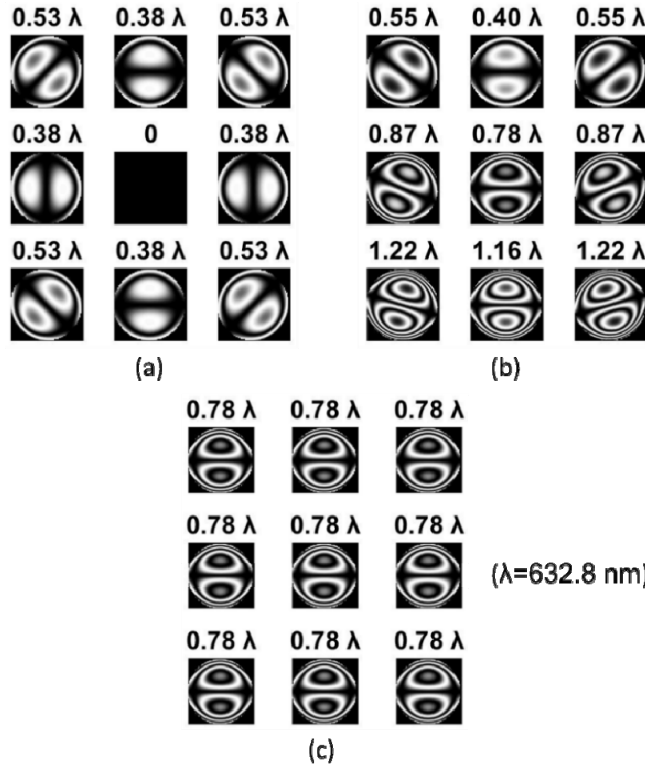$$\left| Z_{7/8} \right| = \sqrt{Z_7^2 + Z_8^2}.$$ (8)

Fig. 13. Simulated interferograms of coma in (a) aligned state, (b) misaligned state, and (c) subtraction of aligned and misaligned states. The adopted wavelength was 632.8 nm.

The Hilbert telescope was a Ritchey–Chrétien optical system, whose third-order coma was initially corrected. In the experimental setup, a parabolic mirror was used off-axis, which induced third-order coma. Thus, the overall optical system was nominally uncorrected for coma. As discussed in Section 2, for the entire system, third-order coma exhibits a null on axis and is field symmetric, field linear at off-axis positions in an aligned state (shown in Fig. 13(a)). In the misaligned state as shown in Fig. 13(b), a 0.5 mm decenter was induced to the secondary mirror of the Hilbert telescope, so the third-order coma continues to be field linear, but the minimum point was displaced to an off-axis position. To further illustrate the coma corrected case, a subtraction of the aligned system to the misaligned system was made at each field point, which cancels out the coma induced from operating the parabolic mirror off-axis, leaving field constant coma as the result of decenter in the secondary mirror of the Hilbert telescope only, as shown in Fig. 13(c). Notably, a proper tilting of the secondary mirror will generate equivalent fringe patterns.

5. Experimental results

The interferograms of Fringe Zernike coma pairs ($Z_{7/8}$) given in Fig. 14(a-c) correspond to simulation fringe patterns shown in Fig. 13(a-c), respectively. Measurements were taken at each field point in the aligned and misaligned states, where measurements were repeated eight

times and averaged at each location. The data processing was done using the QED Toolkit. The central missing area in each interferogram was caused by the combined obscuration from the secondary mirror mount and the tip/tilt mirror assembly. The experiment was carried out in an ordinary optical lab and the interferometer was quite sensitive to air turbulence, thus, measurement errors were inevitable, and a statistical analysis will be given in Section 6.2. In the tolerance of measurement errors, the experiment shows consistent results with the simulations. Let us note that there were multiple fold mirrors between the interferometer and the parabola. These mirrors were likely not in a single plane of symmetry and the out-of-plane tilts rotated the image so that the spiders were not perpendicular to the edge of the detector, even though the interferometer was perpendicular to the table and so were the telescope spiders. However, this residual misalignment had no influence on the magnitude of third-order coma, while merely rotated the entire interferogram on the pupil [15].
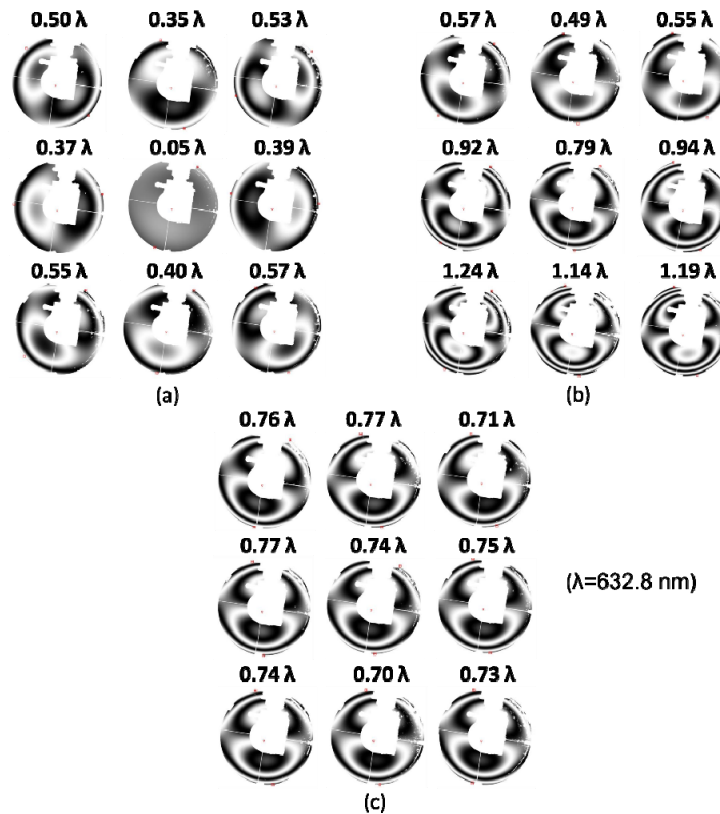
Fig. 14. Experimental results of Fringe Zernike coma in waves units at λ equal 632.8 nm for (a) the aligned system, (b) the misaligned system, and (c) the subtraction of the aligned and misaligned systems.

6. Data analysis

6.1 Accuracy of the Fringe Zernike fit

In the simulation, the pupil map analysis (PMA) in CODE V was utilized to display the wave aberrations in the exit pupil of the experimental setup and the results were fit to Zernike Polynomials [16]. CODE V embeds two types of Zernike polynomials that are Standard Zernike polynomials (ZRN) and Fringe Zernike polynomials (ZFR) that differ in ordering. The polynomial mathematical representation used to describe wavefront aberrations in

commercial interferometers is also based on ZFR or ZRN. Without loss of generality, we adopted ZFR in our PMA and Zernike fit in MetroPro (Software of Zygo interferometer) [17].

Because third-order coma is the investigation in this paper, an error analysis on the estimation of Zernike coma when considering a disk versus an annular aperture is performed to quantify the impact of the obscuration. Figure 15 depicts an illustration of a circular aperture and an annular aperture, in which ρ denotes the normalized pupil coordinate and ε denotes the obscuration ratio. The circular aperture is the special case of the annular aperture case when the obscuration is zero. The orthogonal Zernike annular polynomials for $Z_{7/8}(\rho, \theta, \varepsilon)$ are given in Eqs. (9) and (10) [18] as

$$Z_7 = \frac{3\left(1+\varepsilon^2\right)\rho^3 - 2\left(1+\varepsilon^2+\varepsilon^4\right)\rho}{\left(1-\varepsilon^2\right)\left[\left(1+\varepsilon^2\right)\left(1+4\varepsilon^2+\varepsilon^4\right)\right]^{1/2}}\cos\theta, \qquad (9)$$

$$Z_8 = \frac{3\left(1+\varepsilon^2\right)\rho^3 - 2\left(1+\varepsilon^2+\varepsilon^4\right)\rho}{\left(1-\varepsilon^2\right)\left[\left(1+\varepsilon^2\right)\left(1+4\varepsilon^2+\varepsilon^4\right)\right]^{1/2}}\sin\theta. \qquad (10)$$

When $\varepsilon = 0$, Eqs. (9) and (10) reduce to

$$Z_7 = \rho\left(3\rho^2 - 2\right)\cos\theta, \qquad (11)$$

$$Z_8 = \rho\left(3\rho^2 - 2\right)\sin\theta. \qquad (12)$$

Equations (11) and (12) conform to MetroPro and CODE V. In our case, the outer diameter of the SMA was 100 mm and the clear aperture of the primary mirror was 304.8 mm, which caused a linear obscuration of 33%. When compared with the obscuration caused by the mount of the tip/tilt mirror (28%), a central obscuration of 33% was found to impact the experimental setup. Applying $\varepsilon = 0.33$ and $\rho = 1$ into Eqs. (9) and (10) and calculating the magnitude of $Z_{7/8}$ based on Eq. (8), the result of the Zernike coma fit is 0.961. For a circular Zernike fit using Eqs. (11) and (12) and Eq. (8) when $\rho = 1$, the result of the Zernike coma fit is 1. The error from using the circular polynomials over an annular aperture measurement is estimated at 3.9%.
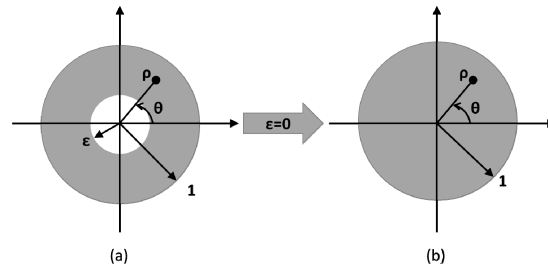

Fig. 15. Geometry illustration of (a) a normalized annular aperture with obscuration of ε and (b) is a normalized circular aperture.

6.2 Statistical analysis of the measurements

Environmental influences that may include air turbulence, vibration and heat will affect the stability of the interferometric measurements. We analyzed the measurements statistically to verify their accuracy and stability. During the data collection, multiple measurements were taken continuously at each field point in the aligned and misaligned states under the same environmental conditions. One group of measurement data, which was taken at the field point $(-0.1°, -0.1°)$ in the misaligned state is discussed here as an example, and results are shown

in Fig. 16(a) for that point in the field. A line chart of the RMS value of the wavefront and Fringe Zernike coma pair ($Z_{7/8}$) from eight consecutive measurements is reported, which indicates that the standard deviation of the RMS wavefront value is 0.02 λ, while the coefficients for Z_7 and Z_8 vary within 0.03 λ and 0.06 λ, respectively, at a wavelength of 632.8 nm. A further analysis was done to all measurement data and reported in Fig. 16(b). The measurements were taken over nine field points under two alignment states, which yielded 18 entries. Each data point consisted of eight measurements. The standard deviations of these 18 entries are listed for the RMS wavefront values, ξ/100 where ξ refers to the angle of the coma interferogram as defined by Eq. (13), and the magnitude of the coma aberration $Z_{7/8}$ defined by Eq. (8). Note that taking a hundredth of the value of ξ helps fitting all quantities on the same plot. The standard deviation in the RMS wavefront values is within 0.04 λ, in the ξ/100 is within 0.09°, and in the magnitude of $Z_{7/8}$ is within 0.06 λ, in which λ stands for 632.8 nm.

$$\xi_{7/8} = \tan^{-1}\left(\frac{Z_8}{Z_7}\right). \tag{13}$$
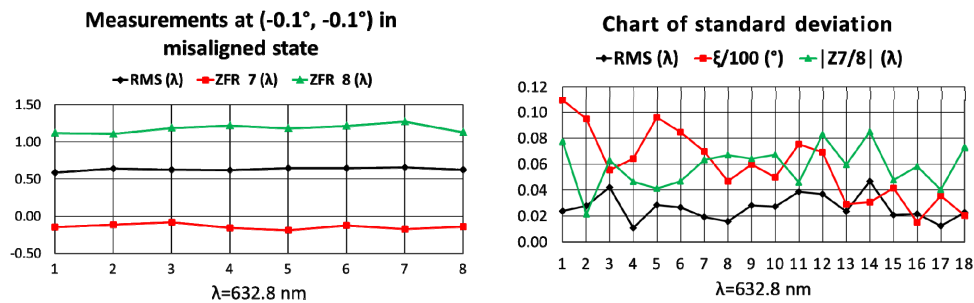
Fig. 16. (a) Statistical analysis of the measurements at field point (−0.1°, −0.1°) in the misaligned state. (b) Standard deviation display of eight consecutive measurement data for that field point reported in three different metrics.

7. Future work

Next step of this study will be the investigation of third-order astigmatism. The theory of NAT has four different pre-conditions for the analysis of third-order astigmatism, which are with and without primary mirror surface figure errors, and with and without misalignment in the system. Details are given in [19–21]. For our case, in a preliminary investigation, figure error in the primary mirror and other components involved in the setup brought non-negligible astigmatism to the measurements. Furthermore, to exhibit binodal astigmatism in the field of view, a field range is required that exceeds the field of view we can generate in the present setup. Limited by these conditions, the experiment setup described in this paper is only capable of presenting the nodal property of third-order coma. A different setup involving the Hilbert telescope is now being conceived and soon realized for the investigation of third-order astigmatism.

8. Conclusion

In this paper, we reported the first experimental investigation of NAT. A customized telescope, the Hilbert telescope was designed and implemented. The characteristics of third-order coma were studied under misalignment of the telescope. The aberrations at nine different field points were measured and results were analyzed statistically to show consistency with the simulation. As NAT predicts, in a perturbed system, third-order coma remains single node and field linear in a nominal coma uncorrected system, while third-order coma displays constant field dependence in a nominally coma corrected system.